Dalton Transactions

PAPER

View Article Online
View Journal

Cite this: DOI: 10.1039/c5dt00924c

Structural and electronic characterization of multi-electron reduced naphthalene (BIAN) cobaloximes†

Owen M. Williams, Alan H. Cowley and Michael J. Rose*

Received 6th March 2015,
Accepted 1st April 2015

DOI: 10.1039/c5dt00924c

www.rsc.org/dalton

Reported here are the syntheses and characterization of cobaloximes that feature a bis(imino)acenaphthene (BIAN) appended ligand. The X-ray crystal structures and spectroscopy (^{1}H NMR or EPR) of the complexes within the series $[Co(aqdBF_2)_2(MeCN)_2]$ (**1**), $[Co(aqdBF_2)(MeCN)_2]^-$ (**2**) and $[Co(aqdBF_2)_2(MeCN)_2]^{2-}$ (**3**, **3′**) are reported and the 3-electron reduced complex $[Co(aqdBF_2)_2(MeCN)_2]^{3-}$ (**4**) has been prepared *in situ* and characterized by ^{1}H NMR spectroscopy. The X-ray crystal structures revealed the presence of a 6-coordinate Co^{II} species (**1**), a 5-coordinate Co^{I} species (**2**), and a 4-coordinate complex (**3**, **3′**). In the case of complex **3**, evidence from single crystal EPR spectroscopy ($g_{\|}$ = 2.017, $g_{\perp}$ = 1.987; <10 G linewidths) in conjunction with DFT calculations indicate that the EPR signal originates from a delocalized ligand-based unpaired spin. The frontier orbitals obtained from DFT calculations on **1**, **2**, **3**, & **4** support the electronic assignments that were observed spectroscopically. The cathodic cyclic voltammogram (CV) of the solvato congener in DMF solution, namely $[Co(aqdBF_2)_2(DMF)_2]$, exhibits three reversible redox events near −1.0, −1.5 and −2.0 V *vs.* Fc/Fc^+. Catalytic proton reduction was observed by CV near the third redox peak. Compared with other cobaloximes (E_{cat} = −1.0 V), the delay of catalytic onset arises from the existence of a series of resonance-stabilized intermediates.

1. Introduction

The term molecular electrocatalysts broadly defines a category of homogenous catalysts, typically organometallic, that usually require access to a reduced state prior to observable catalysis. This type of catalysis is particularly well suited for kinetically difficult transformations for which either reduction or oxidation represents a limiting factor. The hydrogen evolution reaction (HER), oxygen evolution reaction (OER), and carbon dioxide reduction are the most actively studied of these reactions.[1–6] Overall, cobaloximes remain one of the most well studied and widely used classes of HER electrocatalysts.[7,8]

Cobaloximes consist of a central cobalt atom that is ligated by the nitrogen donors of oxime ligands that bridge *via* hydrogen bonds or chemically modified BF_2 or BR_2 bridges.[9] The various stages of cobaloxime catalysis have been investigated by electrochemical methods,[10–13] density functional theory,[14–16] electron paramagnetic spectroscopy,[17] and photophysical techniques.[18,19] Cobaloximes have also been incorporated into heterogeneous systems such as glassy carbon,[20] nickel oxide,[21] carbon nanotubes,[22] and gallium phosphide[23,24] substrates. Furthermore, cobaloximes have been explored in conjunction with homogeneous photosensitizers,[25–28] as components in aqueous systems,[29–31] as a functional catalyst on vesicle membrane surfaces,[32] and used as part of an artificial hydrogenase in a hybrid *Sw*Mb system.[33] Moreover, increasingly elaborate ligand designs have been devised and studied. However, only marginal improvements over the most basic complexes have been realized.[34–36]

The two most widely known and cited cobaloxime case studies are those that involve the dimethyl and diphenyl glyoxime ligands (specifically, $[Co(dmgBF_2)_2(MeCN)_2]$ and $[Co(dpgBF_2)_2(MeCN)_2]$, Fig. 1). Synthesized originally by Schrauzer and Espenson,[37,38] these complexes attracted atten-

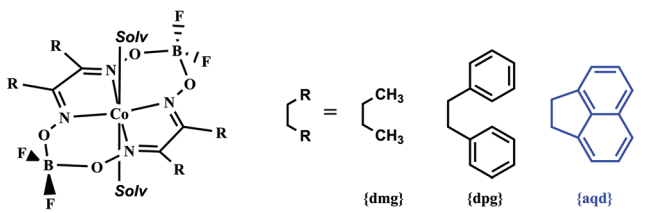

Fig. 1 Cobaloximes studied in the literature and investigated herein.

Department of Chemistry, The University of Texas at Austin, Austin, TX 78712, USA. E-mail: mrose@cm.utexas.edu

† Electronic supplementary information (ESI) available. CCDC 1052415–1052419. For ESI and crystallographic data in CIF or other electronic format see DOI: 10.1039/c5dt00924c

tion as electrocatalysts following seminal work by Peters,[10,12] and Fontecave and Artero.[11,13] In these early reports, the relationship between the backbone substituents (*i.e.* phenyl *vs.* methyl groups) showed that it is the potential of the observed $Co^{II/I}$ redox couple that determines the potential at which the HER reaction takes place. For example, in the case of the fluorinated iron diglyoxime [$Fe(dArFgBF_2)_2(py)_2$], backbone tuning permitted a remarkable change in the $Fe^{II/I}$ reduction potential, while retaining an analogous catalytic cycle.[39] Furthermore, a second redox peak that was detected in the case of [$Co(dmgBF_2)_2(MeCN)_2$] was deemed to be a ligand based redox event.[13] The redox catalysis in this case could be achieved at either redox couple by an appropriate choice of acid. However, the structure and electronics of this doubly reduced species remain to be explored. As a consequence, these reports stimulated our interest in incorporating a more redox active backbone.

Bis(imino)acenaphthene (BIAN) ligands have proven to be useful for a variety of catalytic systems, that range from C–C bond coupling to polymerization.[40] In particular, the naphthalene backbone of this ligand facilitates a rich redox chemistry.[41–45] Moreover, the bis(diisopropyl)phenylimino ligand (dpp-BIAN) is capable of undergoing four successive one-electron reductions.[41] Furthermore, the ease of preparation of BIAN complexes allows for the incorporation of a wide variety of Schiff bases.[46] Accordingly, we became interested in incorporating the BIAN motif into a known electrocatalytic system. Overall, cobaloximes exhibit three attributes that render them desirable for a study of a BIAN appendage, namely: (i) the capability for electrocatalytic activity, (ii) suitable axial binding sites for the substrates, and (iii) a ligand framework that is compatible with BIAN derivatization.

The present work is focused on an analogous BIAN-cobaloxime, along with the X-ray crystal structures of several multi-electron reduced species. The foregoing examples were characterized spectroscopically and also by means of DFT calculations. An overview of the electrocatalytic studies (cyclic voltammetry and bulk electrolysis) of this complex is also presented below.

2. Results

2.1. Electrochemistry

The cyclic voltammogram for the corresponding solvato complex in DMF solution, namely **1**·DMF_2, is displayed in Fig. 2. This complex exhibits a reversible feature at −0.95 V *vs.* Fc/Fc^+ ($\Delta E_p \approx 100$ mV), thereby generating [$Co(aqdBF_2)_2(DMF)]^-$. This response is almost identical to that of the $Co^{II/I}$ reduction potential that was reported for [$Co(dmgBF_2)_2(DMF)_2$] ($E_{1/2} \approx -1.0$ V *vs.* Fc/Fc^+).[13] The ensuing cathodic sweep revealed two additional reversible features at −1.56 and −2.00 V *vs.* Fc/Fc^+ ($\Delta E_p \approx 60$ mV in both cases). Each feature exhibits a linear increase in current with respect to scan rate (Fig. 2, inset; see Fig. S1† for full CV traces), thus confirming the occurrence of homogeneous processes in each case. As a consequence, the reduced species are formulated as [$Co(aqdBF_2)_2(DMF)]^-$, [$Co(aqdBF_2)_2]^{2-}$, and [$Co(aqdBF_2)_2]^{3-}$. The reducing equivalents in the latter two complexes are absorbed by the ligand framework.

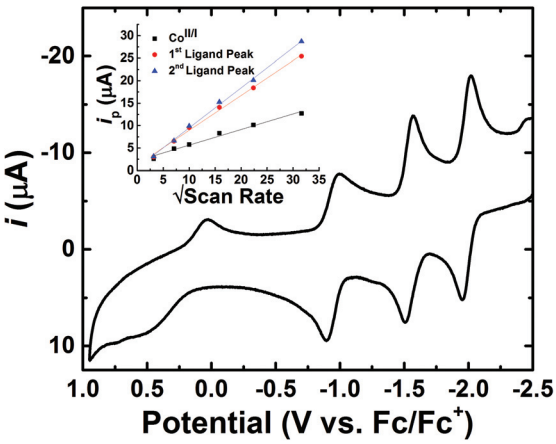

Fig. 2 Cyclic voltammogram of **1**·$(DMF)_2$ obtained under an N_2 atmosphere in a DMF electrolyte solution (0.1 M NBu_4PF_6). Experimental conditions: 100 mV s^{-1}; WE: GC, RE: Ag, CE: Pt. Inset: scan rate dependence for each cathodic feature, indicating homogeneous processes in each case.

2.2. Chemical reductions

To help probe this rich redox chemistry, a series of chemical reductions were performed with the objective of accessing the putative complexes that had been detected in the cathodic cyclic voltammogram. The stable, one-electron reduced species was produced *via* the reaction of the parent cobaloxime with a near stoichiometric quantity of sodium naphthalide (1.2 equivalents, $E \approx -3.10$ V *vs.* Fc/Fc^+)[47] in THF, thus yielding a stable bluish-violet solution. Re-dissolution of the solid product in an MeCN solution containing excess 12-crown-4 afforded a violet colored solution. The crystalline product was isolated by vapor diffusion of Et_2O into an MeCN solution to afford the five-coordinate, square pyramidal product [$Na(12\text{-crown-4})_2$][$Co(aqdBF_2)_2(MeCN)$] (**2**). Further details are provided in the X-ray crystallographic section. The difficulties that were encountered in obtaining pure **2** in significant yields prompted a search for an alternative method of generating the singly reduced species. Regardless of stoichiometry, cobaltocene reduction ($E \approx -1.3$ V *vs.* Fc/Fc^+)[47] resulted in the generation of a purple solution in acetonitrile, which was indicative of a one electron reduction. The assignment was corroborated on the basis of single crystal XRD (Fig. S2†) and ^1H NMR spectroscopy.

The two-electron reduced species was isolated by treatment of a solution of the parent cobaloxime **1** with an excess potassium graphite (>3 equivalents, $E = -2.90$ V *vs.* Fc/Fc^+)[47] in THF, thus forming a dark navy blue solution that was markedly different from the violet colored solution that had been observed for the corresponding one-electron reduced complex.

Extraction of the product into a MeCN solution containing dibenzo-18-crown-6 afforded $[K(dibenzo\text{-}18\text{-}crown\text{-}6)]_2[Co(aqdBF_2)_2]$ (**3**), which features the presence of a cobalt center in a square planar geometry (*vide infra*, X-ray Crystallography section). A similar procedure was found to be effective for the isolation of the alkyl crown congener **3** of formula $[K(18\text{-}crown\text{-}6)]_2[Co(aqdBF_2)_2]$. Finally, the preparation of the three-electron reduced compound (**4**) was carried out by the treatment of **1** with an excess of Na/Hg ($E \approx -2.4$ V *vs.* Fc/Fc^+) in a THF solution in the presence of an excess of 12-crown-4. It is important to note that the green solution is not observed in the absence of a supporting crown ether. The role of the alkali-crown complex in stabilizing the reduction state of the complex is highlighted in the X-ray crystallography section.

Overall, an evaluation of the reduction potentials and stoichiometries of the reductants that were employed failed to reveal a coherent trend regarding the isolated products (among $NaC_{10}H_8$, KC_8, Na/Hg, all have a reduction potential cathodic of -2.0 V *vs.* Fc/Fc^+). The $CoCp_2$ reduction clearly shows a dependence on potential since it only leads to the singly reduced product regardless of stoichiometry. Inspection of the X-ray crystal structures (*vide infra*) revealed the presence of secondary effects due to the interaction of the alkali metals with the complex that represent a determining factor in terms of the identity of the final product. For example, reduction of the parent complex with $NaC_{10}H_8$, KC_8, or Na/Hg in neat THF each generate blue solutions that are indicative of the formation of the 2-electron reduced species. However, subsequent extractions of the various alkali salts into MeCN–crown ether mixtures (to aid solubility and crystallization) produced different results. For example, dissolution of the Na salt of the 2-electron reduced blue species in an MeCN–12-crown-4 mixture caused an immediate color change from blue to violet, (which is indicative of an auto-oxidation process) and resulted in the formation of the 1-electron reduced species **2**. By contrast, extraction of the K salt of the 2-electron reduced blue species into a MeCN solution that contained 18-crown-6 derivative retained the blue color, which subsequently proceeded to generate the authentic crystalline samples of the 2-electron reduced species **3**.

Interestingly, a distinct reductive behavior was evident in THF solution that depended on the presence or absence of a crown ether. In contrast to the blue solutions that were apparent in the absence of the crown ether, the reduction of **1** with Na/Hg in a THF solution that contained 12-crown-4 resulted in the formation of a green solution, which was indicative of the presence of the 3-electron reduced species **4**. Overall, the X-ray crystal structure data revealed the presence or absence of site-specific interactions between the crowned Na^+ or K^+ ions with the oxime-N/O or BF_2 moieties. Evidently, it is this counterion cooperativity that represents a critical factor in terms of stabilizing the reduced states during isolation. Furthermore, it is clear that careful attention must be paid to the presence (or absence) and identity of the supporting alkali-crown species.

2.3. X-ray crystal structures

2.3.1 Ligand (aqdH2). The X-ray crystal structure of the parent ligand, acenaphthenequinone dioxime ($aqdH_2$, Fig. S3†) exhibited structural parameters that are consistent with those of other BIAN-Schiff base ligands. Moreover, the C=N bond lengths of 1.285(2) and 1.286(2) Å are consistent with the presence of double bond character and the C–C bond length of 1.502(3) Å is in agreement with the value expected for a single bond. The N1–C1–C2–N2 torsion angle of 6.6(2)° is most likely due to the constrained five membered ring of the acenaphthene framework. All other bond distances fall within the expected ranges.

2.3.2 $[Co(aqdBF_2)_2(MeCN)_2]$ (1). The X-ray structure of **1** (Fig. 4) revealed the presence of a Co^{II} ion in a pseudo-octahedral geometry. This outcome was anticipated for a cobaloxime of this type that had been crystallized from a coordinating solvent (MeCN). Furthermore, the axial MeCN ligands are tilted away from a linear orientation by 14.8°, and each MeCN molecule is flanked by a BF_2 bridge that is tilted up or down out of the plane of the macrocycle in order to avoid the axial ligand. The structure of the $aqdBF_2$ ligand of **1** is essentially planar, as evidenced by the torsion angle of 1.4(1)° for the C2–C1–N1–Co1 chain. The $Co–N_{ox}$ bond distances of 1.896(1) Å for **1** (fourfold crystallographic symmetry) are slightly longer than those found for closely related cobaloximes $[Co(dmgBF_2)_2(MeCN)_2]$ (1.878(1), 1.881(2) Å)[17] and $[Co(dpgBF_2)_2(MeCN)_2]$ (1.881(3), 1.889(3) Å).[12] The foregoing results are likely to be a consequence of the expanded N=C–C=N bite angle in the fused naphthalene ring system, which results in N–Co–N angles of 84.66(4)° for aqd, *versus* 81.70(7)° for dmg or 81.8(1)° for dpg. The axial $Co–N_{MeCN}$ distances of 2.2712(2) Å are also longer than those found in the $dmgBF_2$ and $dpgBF_2$ congeners (2.253(2), 2.241(3) Å). However, the C=N and C–C bonds in the macrocycle (1.293(1) and 1.488(2) Å) are commensurate with those of the neutral ligand (1.286(2), 1.285(2) and 1.502(2) Å). Furthermore, the acene C–C bond distance in **1** (1.488(2) Å) is very close to that observed for the free ligand (1.502(2) Å), thus indicating that no electronic change or significant delocalization of charge from the cobalt(II) center to the ligand framework is observable by XRD.

2.3.3 $[Na(12\text{-}crown\text{-}4)_2][Co(aqdBF_2)_2(MeCN)]$ (2). The cobalt center in this species adopts a square based-pyramidal structure, which effects a 0.415 Å displacement of the cobalt ion out of the equatorial plane and a significant contraction of the single axial $Co–N_{MeCN}$ bond to 2.007(3) Å, as compared with the two axial $Co–N_{MeCN}$ bonds (2.2714(16) Å)) that were observed in the case of the parent complex. A comparison of the structural parameters of **2** with those of the reduced diphenyl (dpg) cobaloxime analog $[Na(12\text{-}crown\text{-}4)_2][Co(aqdBF_2)_2(MeCN)]$ reveals that the bond lengths are very similar ($N–Co_{avg}$ 1.851 Å; $C=N_{avg}$ 1.321 Å; $C–C_{avg}$ 1.457 Å).[12] However, within the ligand framework there is a slight contraction of the N–Co bond length (~0.016 Å), an elongation of the N–C bond length (~0.017 Å), and a contraction of the C–C bond length (~0.040 Å) in comparison with that of **1**. The slight differences

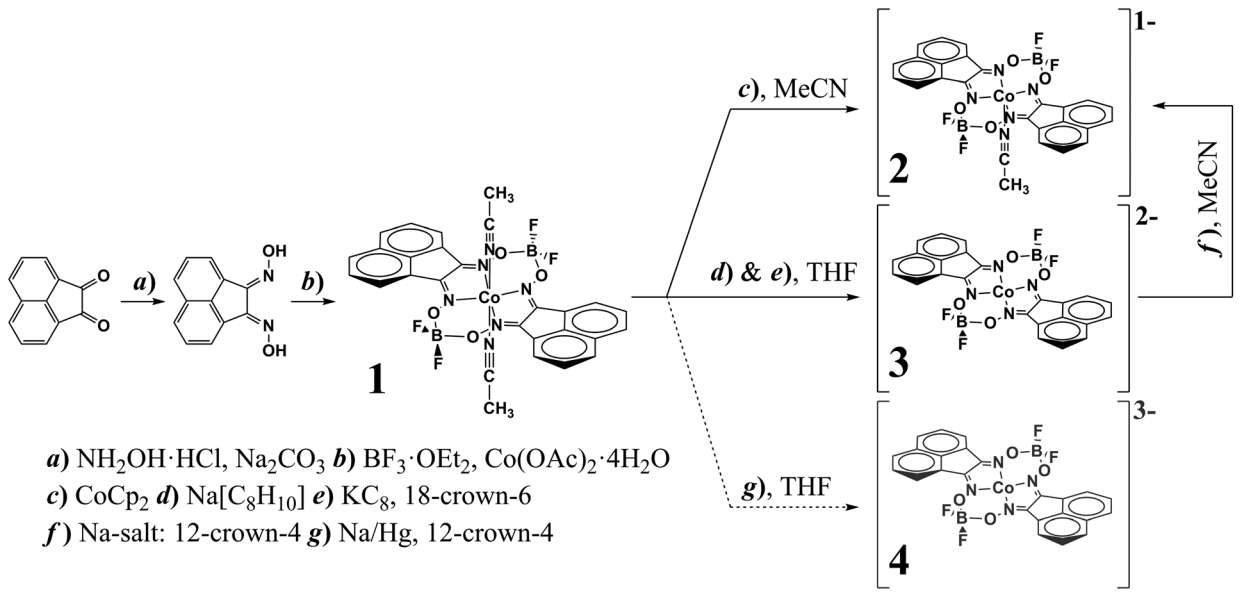

Fig. 3 Synthetic route for the ligand aqdH$_2$, **1** and the chemically reduced species **2**, **3** and **4**.

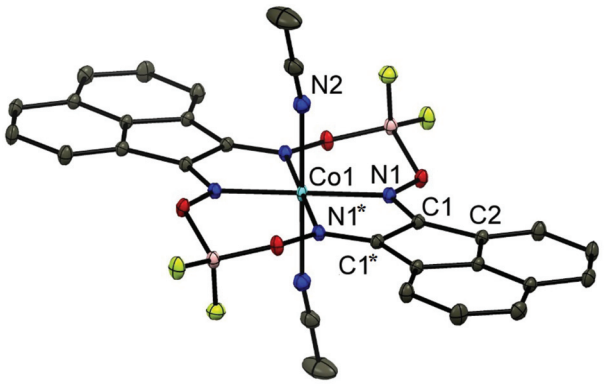

Fig. 4 ORTEP diagram (50% thermal ellipsoid plots) of the parent complex [Co(aqdBF$_2$)$_2$(MeCN)$_2$] (**1**). All hydrogen atoms have been omitted for clarity. Selected bond lengths (Å) and angles (°): N1–Co1, 1.8961(9); N2–Co1, 2.271(2); C1–N1, 1.293(1); C1–C1*, 1.488(2); N1–Co1–N1*, 84.66(4).

in the C–N and C–C bond distances between **1** and **2** may indicate partial delocalization of the reducing electron onto the N–C–C–N fragment. The bond lengths, however, show altered parameters when compared with that of a model one-electron reduced BIAN, namely the sodium complex of diisopropylphenyl-BIAN (dpp-BIAN). In comparison with Na-dpp-BIAN, complex **2** exhibits slightly shorter C=N (~1.310 *cf.* 1.328 Å) and slightly longer C–C (~1.448 *cf.* 1.446 Å) bond distances.[41] However, due to the significant change in the coordination environments of **1**, **2**, and [Na][dpp-BIAN] it is difficult to assign formal ligand charges and/or metal oxidation states based solely on structural data.

2.3.4 [K(dibenzo-18-crown-6)]$_2$[Co(aqdBF$_2$)$_2$] (3). The structure of the doubly reduced complex, **3** (Fig. 5, center) revealed an increase of the planarity of the entire macrocycle in comparison with that of the singly reduced (Na salt) structure (24.01 *cf.* 47.52 degrees for the mean plane angle between the naphthalene backbone units). This outcome is likely a consequence of the orbital overlap required for effective delocalization of the additional electron. The cobalt center in this compound adopts a square planar structure, and is accompanied by a further contraction of the N–Co bond length (~0.024 Å), an elongation of the N–C bond length (~0.030 Å), and a lengthening of the C–C bond (~0.012 Å) in comparison with those of the singly reduced species. Of particular note are the short contacts between the two chelated potassium cations and the fluorine atoms (K···F = 2.621(2), 2.655(2) Å) on the BF$_2$ moieties (Fig. 5, bottom center). The open-face chelation of the K$^+$ ion by dibenzo-18-crown-6 provides coordination sites for the direct interaction of the alkali metal with the electronegative moieties on the cobalt macrocycle. In contrast, the bis-chelated nature of the sodium counterion [Na(12-crown-4)$_2$] found in **2** precluded any direct interaction between the alkali metal and the cobaloxime. As noted in the Chemical Reductions section (*vide supra*), it can be inferred that such a direct contact with the K$^+$ ion in **3** (and **3′**, see below) stabilizes the reduction state of the complex thereby preventing auto-oxidation (see Fig. 3).

2.3.5 [K(18-crown-6)]$_2$[Co(aqdBF$_2$)$_2$] (3′). In a similar fashion to **3**, the 18-crown-6 ligated K$^+$ salt, **3′** displayed the same square planar geometry at the cobalt center, with close contact between the crown-stabilized cation and the cobaloxime (Fig. 5, bottom right). Examination of the structure of **3′** revealed that the potassium cations interact with the macrocycle in a different manner, such that each [K(18-crown-6)]$^+$ unit adopts close contacts with a lateral set of two N–O frag-

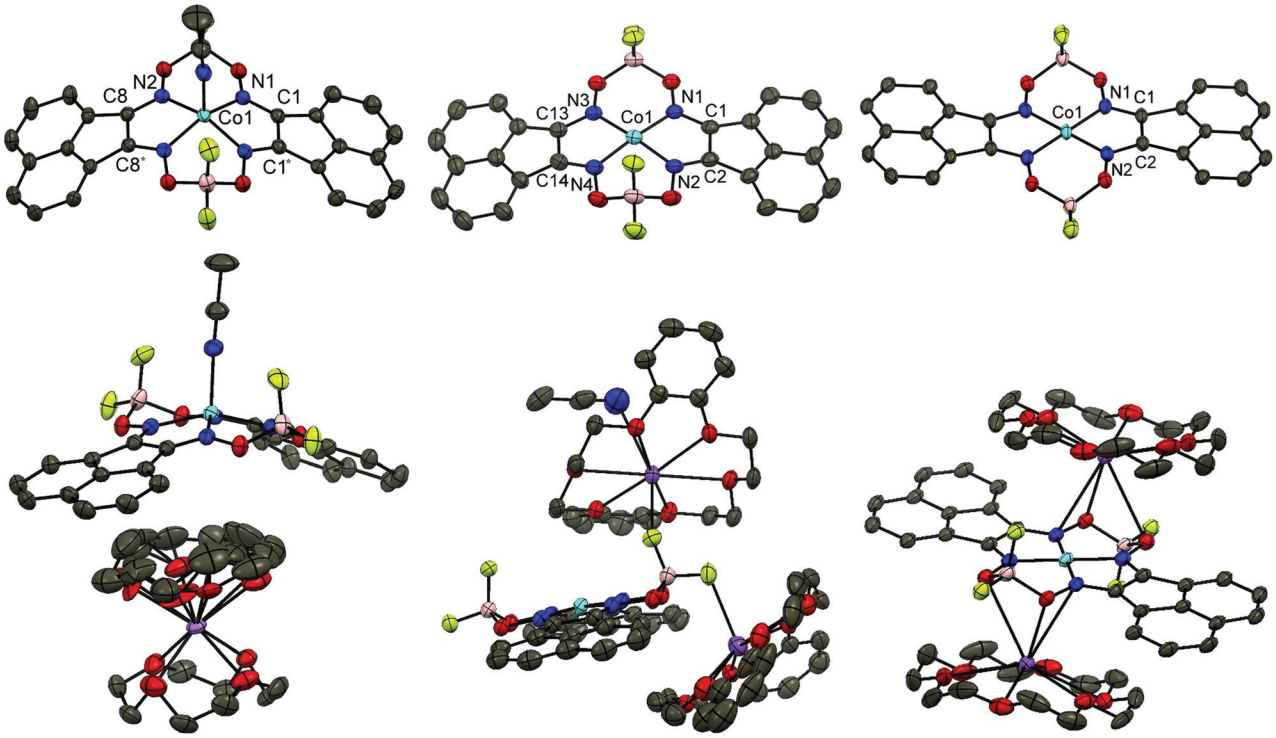

Fig. 5 X-ray crystal structures of **2**, **3**, & **3′** (50% probability thermal ellipsoids). (top) Only the cobalt-containing anions are displayed, and hydrogen atoms, counterions, and solvent molecules have been omitted for clarity. (bottom) Full structures, cation inclusive are shown below. Selected bond lengths (Å) and angles (°), with symmetry generated atoms are designated by an asterix (*): $[Co^{I}(aqdBF_2)_2(MeCN)]^{-}$: N1–Co1, 1.879(2); N2–Co1, 1.887(2); C1–N1, 1.311(2); C8–N2, 1.308(2); C1–C1*, 1.439(3); C8–C8*, 1.445(3). $[Co^{I}(aqdBF_2)_2^{\bullet-}]^{2-}$, dibenzo-18-crown-6 potassium salt: N1–Co1, 1.863(2); N2–Co1, 1.862(2); N3–Co1, 1.859(2); N4–Co1, 1.854(2); C1–N1, 1.339(3); C2–N2, 1.333(4); C13–N3, 1.344(3); C14–N4, 1.335(4); C1–C2, 1.460(4); C13–C14, 1.455(4). $[Co^{I}(aqdBF_2)_2^{\bullet-}]^{2-}$, 18-crown-6 potassium salt: N1–Co1, 1.847(2); N2–Co1, 1.834(2); C1–N1, 1.328(3); C2–N2, 1.326(3); C1–C2, 1.326(3).

ments (an η_4 arrangement) on the macrocycle (K⋯O = 2.896(2), 3.121(2) Å; K⋯N = 3.160(2), 3.400(2) Å). The overall closer approach of the entire $[K(18\text{-crown-6})]^{+}$ fragment to the cobaloxime that was observed in **3′** is a consequence of the less bulky, alkyl framework of the crown in **3′** compared with that of the dibenzo-crown framework in **3**. Furthermore, the planarity of **3′** was found to have increased in comparison with that of its congener, **3** (N–Co–N ~180° *cf.* 173°). Interestingly, the increased planarity of **3′** occurs in conjunction with an '*anti*' orientation of the BF_2 groups, whereas the BF_2 linkers in **3** adopt a '*syn*' conformation. The relevant metrical parameters for this complex are comparable to those that were found for **3**, albeit with slightly decreased N–Co bond lengths (~0.018 Å), shorter C=N bonds (~0.016 Å), and acenaphthene C–C bonds (~0.015 Å). The discrepancies are attributable to the planar orientation of the ligating moieties.

2.4. Spectroscopic characterization

2.4.1 EPR of $[Co(aqdBF_2)_2(MeCN)_2]$ (1). The EPR spectrum of crystalline **1** was obtained by means of a solid state powder measurement at 85 K, the overall result of which is displayed in the upper panel of Fig. 6. This spectrum is indicative of the presence of a low-spin, axial system as expected for the d^7 Co^{II} ion in **1** supported by the planar $(aqdBF_2)_2$ macrocycle, and coordinated by the two axial MeCN ligands. The simulated EPR signal aligned well with that of the experimental spectrum, thus corroborating the features that were apparent in the range of $g \approx 2$–2.3 ($g_x = 2.29$, $g_y = 2.20$, $g_z = 2.02$). The result is also consistent with the solid state magnetic susceptibility measurement that was performed on a crystalline sample of **1** ($\mu_{eff} = 1.71\mu_B$, 298 K; predicted $\mu_{SO} = 1.73\mu_B$). Overall, the EPR spectrum of **1** is very similar to those reported for $[Co(dmgBF_2)_2]$ in similar environments ($g_x = 2.26$, $g_y = 2.17$, $g_z = 2.01$ $A_z = 338$ MHz).[17] However, the anticipated ^{59}Co ($I = 72$) hyperfine pattern was not evident in the solid state measurement. This outcome is most likely due to the close proximity of the paramagnetic centers in the crystalline state. However, in a frozen solution of MeCN–THF (10% v/v) at 85 K, complex **1** exhibited a significantly more resolved spectrum (Fig. 6, bottom panel) with primary features at $g_x = 2.31$, $g_y = 2.26$, $g_z = 2.02$. The latter outcome is also indicative of the presence of a low-spin d^7 ion in solution; no features near $g \approx 4.3$ were observed. Furthermore, the solution phase EPR spectrum of **1** exhibited the anticipated eight-line pattern for the $I = 72$ ^{59}Co nucleus, with a coupling constant of $A_z = 110$ G (~310 MHz). The correlation of the hyperfine splitting pattern

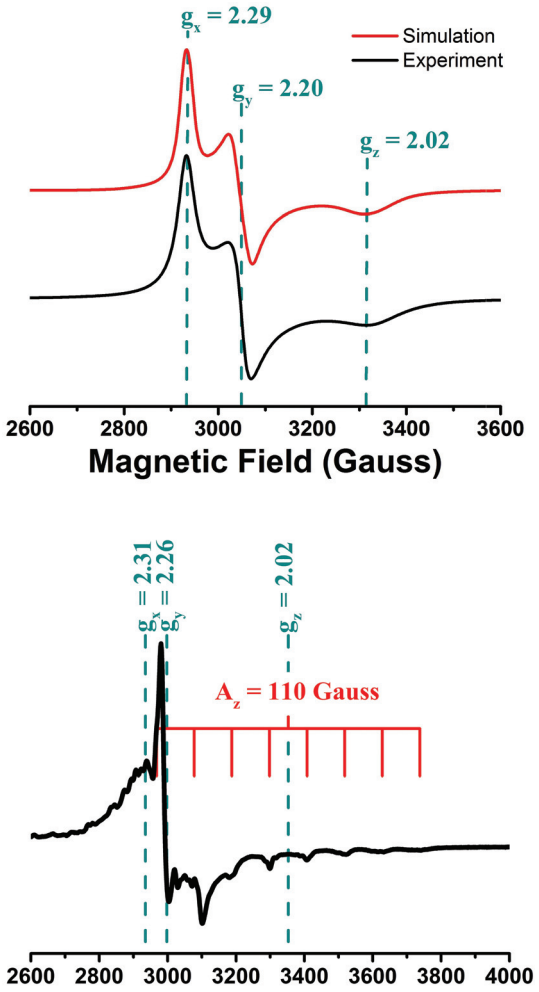

Fig. 6 X-band EPR studies of $[Co(aqdBF_2)_2]$ (**1**). Top Panel: (Black line) powder EPR spectrum of a solid sample of **1** at 85 K; (red line) simulated EPR spectrum; simulation parameters: g_x = 2.29, g_y = 2.20, g_z = 2.02. Bottom panel: X-band EPR spectrum of **1** in a frozen glass of 10% MeCN–THF (v/v). Instrument parameters, powder spectrum: frequency, 9.40 GHz; modulation, 100 kHz; power, 0.2 mW; field modulation, 2 G. Instrument parameters, solution spectrum: frequency, 9.44 GHz; modulation, 100 kHz; power, 25 mW; field modulation, 10 G.

with the g_z = 2.02 feature is consistent with the primary orientation of the unpaired spin being aligned along the z axis, as expected for the singly occupied d_{z^2} orbital. This interpretation is also consistent with the long Co–N_{MeCN} bond distances (2.2714(16) Å) that were evident in the crystal structure of **1**.

2.4.2 ^{1}H NMR of $[CoCp_2][Co(aqdBF_2)_2(MeCN)]^-$ (2′). Following the isolation as the Na-crown salt, the re-dissolution of **2** in CD_3CN resulted in slow bleaching of the solution. This outcome is possibly due to interaction of the residual moisture from the CD_3CN solvent with the reduced species, which, in turn could result in hydrolysis of the complex. The decomposition of the complex in CD_3CN is not due to an inherent instability or reactivity of the complex since **2** was easily extracted into and crystallized from CH_3CN during the isolation process. In order to circumvent this limitation, an analogous reduction was performed with cobaltocene, which afforded the cobaltocenium salt, **2′**. The prevalent signals emanate from the one electron reduced species, and exhibit resonances that correspond to those of the cobaloxime anion and the cobaltocenium cation. Identification of the anion as the desired product was confirmed by means of a single crystal X-ray diffraction study (Fig. S2†). The anion that resulted from this one-electron reduction afforded a stable CD_3CN solution of the desired complex (Fig. 7). The ^{1}H NMR spectrum of this cobaltocenium salt revealed the presence of a diamagnetic species that exhibited two doublets (δ = 8.15 ppm, J = 6.8 Hz; δ = 7.92 ppm; J = 8.0 Hz) along with a doublet of doublets (δ = 7.56 ppm, J = 6.8, 8.0 Hz) in the aromatic region, thus confirming the presence of the naphthalene backbone. In comparison with the ^{1}H NMR spectrum of the free $aqdH_2$ ligand (δ = 12.36 ppm, singlet; δ = 8.35 ppm, doublet, J = 6.6 Hz;δ = 8.01 ppm, doublet, J = 7.8 Hz; δ = 7.70 ppm, doublet of doublets, J = 6.8, 8.0 Hz), these resonances show only a slight shift in the aromatic region, signifying that little to no change had taken place in the electronic environment of the naphthalene rings.

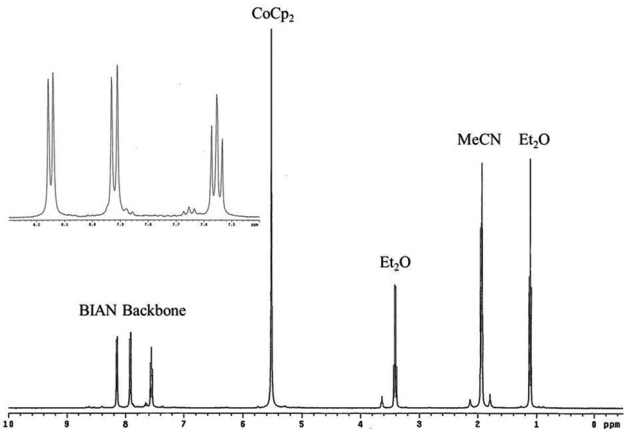

Fig. 7 ^{1}H NMR spectrum of $[CoCp_2][Co(aqdBF_2)_2(MeCN)]$ (**2′**) in CD_3CN at 298 K (400 MHz). The complex was prepared from cobaltocene and structurally characterized as the cobaltocenium salt (Fig. S2†).

2.4.3 EPR of $[K(dibenzo\text{-}18\text{-}crown\text{-}6)]_2[Co(aqdBF_2)_2]$ (3). Solution phase EPR measurements of **3** in either frozen MeCN or MeCN–tol glass (85 K) revealed a broad feature (~100 G linewidth) centered near $g \approx 2.0$ (Fig. 8, top). In contrast, the single crystal EPR spectrum of **1** at 85 K (Fig. 6, bottom) featured a single, extremely sharp peak (linewidth <10 G) with a g-value that systematically ranged between 1.987 and 2.017 depending on the orientation of the crystal. The intensity of this feature increased as the resonance shifted to lower magnetic fields upon rotation of the sample tube. Furthermore, the intensity increased approximately two-fold, thus supporting the assignments of $g_\perp$ = 2.017 and $g_\parallel$ = 1.987 and indicating the presence of an axially anisotropic radical. The proximity of this single feature to the free electron value (g = 2.023), along with the extremely narrow linewidth, strongly suggested the presence of a primarily organic radical. The discrepancy between the line

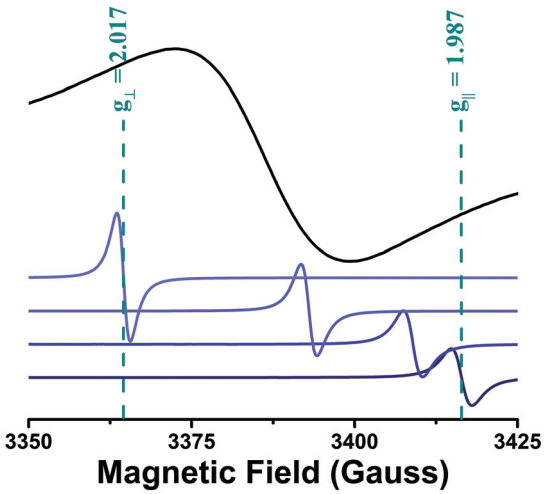

Fig. 8 EPR studies of $[K(dibenzo\text{-}18\text{-}crown\text{-}6)]_2[Co(aqdBF_2)_2]$ (**3**): (top) solution EPR spectrum obtained in frozen MeCN at 85 K; (bottom) single crystal EPR of **3** obtained at 85 K during a 90° rotation using a controlled angle goniometer. Instrument parameters, solution spectrum: frequency, 9.44 GHz; modulation, 100 kHz; power, 20 mW; field modulation, 0.1 G. Instrument parameters, single crystal spectra: frequency, 9.45 GHz; modulation, 100 kHz; power, 10 mW; field modulation, 0.1 G.

widths of the single crystal and frozen-solution measurements can be accounted for by assuming random orientations (and an average of the signals) in the case of the frozen solution. This is further corroborated by a polycrystalline measurement, which showed a complex spectrum, with no discernible pattern upon rotation (see Fig. S4†). The assignment of the additional electron as an organic based radical was supported by DFT calculations that were carried out on complex **3** (*vide infra*, DFT Calculations section).

2.4.4 ^{1}H NMR spectrum of $[Co(aqdBF_2)_2]^{3-}$ (4). The three-electron reduced compound **4** was characterized on the basis of ^{1}H NMR spectroscopy. This complex was generated *in situ* in d^8-THF solution by reduction with Na/Hg in the presence of 12-crown-4. This reaction resulted in the formation of a green solution that could be analyzed (298 K) by ^{1}H NMR. The diamagnetism of **4** was confirmed by the presence of sharp peaks in the aromatic region. As expected for the acenaphthene framework, a pattern of two doublets (δ = 8.21 ppm, J = 7.6 Hz; δ = 7.61 ppm, J = 8.4 Hz) and one triplet (δ = 7.44 ppm, J = 8.0 Hz) was observed. Overall, these resonances are quite similar to those of the one-electron reduced species **2′**, which exhibits such features at δ = 8.15, 7.92 and 7.56 ppm.

2.5. DFT Calculations

Density functional theory calculations were performed with the view of confirming the electronic structures that had been proposed for the reduced cobaloxime complexes (Fig. 9). The geometry optimizations were performed using the X-ray structure coordinates of **1**, **2**, and **3**. The optimized structure of **1** (S = 1/2) closely mimics that of the crystal structure, albeit with a slight reorientation of the axial acetonitrile solvent. The frontier orbital (SOMO) of this particular compound showed evidence of the presence of an unpaired spin located in the d_{z^2} orbital of the metal center. Accordingly, this result confirmed the assignment that had been made based on the EPR results that were discussed earlier.

The frontier orbital (HOMO) of **2** shows a pairing of the electrons in the d_{z^2} orbital. This in turn accounted for the diamagnetism observed for the one electron reduced complex. There is clear evidence for overlap between this orbital and the p_z orbitals located on the nitrogen atoms. This overlap may account for the changes in bond distances that were detected in the X-ray crystal structure. Furthermore, the location of the additional electron confirms that only a small change had taken place in the electronic environment of the acenaphthene backbone.

The frontier orbital (SOMO) and spin density plots (Fig. S5†) that were obtained for **3** indicate that the unpaired spin is located in an orbital that spans the metal center and is primarily delocalized across the two N–C–C–N fragments (S = 12). Interestingly, the spin density also extended slightly onto the glyoximato-O. An extended view of the spin density revealed that the spin density encapsulates the central cobalt ion, but is only slightly localized on the metal center. By contrast, at this isosurface value the ligand framework is replete with spin density. Unrestricted DFT calculations showed a similar alpha spin density plot, albeit accompanied by signifi-

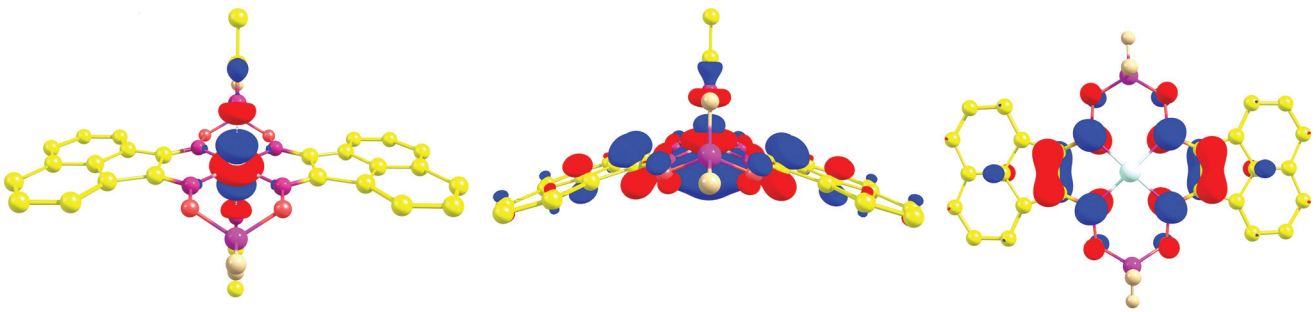

Fig. 9 DFT calculated frontier orbitals for **1**–**3** (left to right) using the B3P86 functional in conjunction with a Wachters/TZVP hybrid basis set; geometry optimizations were performed with a smaller basis set (see Experimental). The surfaces are displayed at the 0.05 isosurface value. Spin density plots for **3** are available in the ESI.†

cant spin contamination ($S_{calc}^2 \approx 1.00$; $S_{exp}^2 = 0.75$). This may indicate that contributions from both $Co^{I}L^{\bullet -}$ and $Co^{II}L^{2-}$ are feasible for this particular compound.

2.6. Electrocatalysis

The proclivity of the title complex for proton reduction was also explored. For this purpose, CV titrations were performed along with additions of two commonly used proton sources, namely *p*-toluenesulfonic acid [TsOH is dissociated, the functional acid is DMF-H^+] and benzoic acid ($PhCO_2H$). The overpotentials for H^+ reduction were determined by the first derivative method described by Fontecave and Artero.[48] Interestingly, the addition of TsOH failed to result in any increase in current at the $Co^{II/I}$ redox couple, a process that is otherwise observed for the majority of cobaloximes. Alternatively, low concentrations of TsOH (2.5 mM) effect a significant increase in current at the third redox event (i_{max}/i_p = 5.77), which is one full volt cathodic of the $Co^{II/I}$ redox potential. At further cathodic potentials (−2.5 V), a related hydritic cobalt intermediate (tentatively assigned) also displayed a reversible peak. At higher concentrations of TsOH (up to 25 mM), the catalyzed $2H^+ \rightarrow H_2$ transformation was evidenced by a significant increase in current (i_{max}/i_p = 43.3, 25 mM, Fig. 10) at −2.3 V *vs.* Fc/Fc^+, which corresponds to a rather high overpotential (η_{TsOH} = 1.5 V, Fig. S6†). By contrast, when $[Co(dmgBF_2)_2(DMF)_2]$ was monitored with a similarly strong acid (HBF_4) in DMF a low overpotential of η = 0.4 V was determined.[12]

An analogous set of experiments with the weaker acid $PhCO_2H$ (10 mM) revealed a surprisingly similar increase in current at the third redox event (i_{max}/i_p = 6.06). However, a catalytic wave was not observed until −2.5 V *vs.* Fc/Fc^+ (i_{max}/i_p = 20.0, Fig. 10). The acid concentration dependence for $PhCO_2H$ is indicative of homoconjugation (η_{PhCO_2H} = 1.1 V, Fig. S7†) as expected for the presence of a carboxylic acid in an organic solvent. The linear dependence of the scan rate *versus* peak current for the CVs that were carried out in the presence of $PhCO_2H$ suggests that these processes are homogeneous (Fig. S8†).

Bulk electrolysis (BE) experiments were attempted in a custom H-cell (Fig. S9†). In any given experiment, a large amount of current was found to pass during the electrolysis, and the hydrogen production was detected by GC. The subsequent rinse tests, however show a similar efficiency for the used electrodes. This similarity of currents can be attributed to native electrode surface reactions, catalyst degradation, metal deposition, and/or solvent degradation. Such processes are more prevalent over the extended time periods associated with bulk electrolysis. The extreme potentials required to observe (by CV) a catalytic response render the analysis of catalytic capability difficult. While no comprehensive study of acids has been performed in DMF as in the case of MeCN,[49] it is likely that these experiments are being performed near or beyond the edge of the useful potential window ($E_{BE} < E_{inf.}$) for each acid. In comparison with the literature cobaloximes, the limitations regarding the operating potential for proton reduction in this particular case are evident. Furthermore, the stabilities of some of the complexes that have been used in bulk electrolysis experiments have been called into question recently.[50,51]

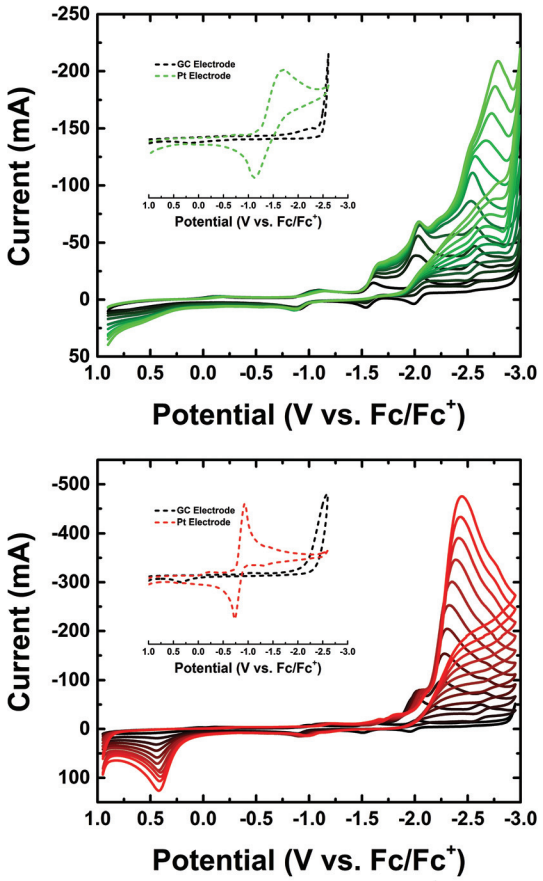

Fig. 10 CV studies of 1·$(DMF)_2$ in the presence of a weak acid (benzoic acid, top) or in the presence of a strong acid (tosic acid, bottom). Insets show the *I*–*V* response in the presence of a 25 mM concentration of the respective acid using either a glassy carbon (black dashed) or platinum (color dashed) button electrode. Standard experimental conditions: 100 mV s^{-1}; WE: GC, RE: Ag, CE: Pt.

3. Conclusions

1 The BIAN redox reservoir acts as an effective electron sink during multiple-electron reduction.

2 During isolation of the reduced species with alkali-based reductants, there is a critical dependence on the presence *versus* absence, as well as the identity of the crown ether employed. In general, complete sequestration of the alkali metal from the reduced complex results in auto-oxidation processes during extraction and crystallization.

3 In contrast, crown-ethers that allow for direct contact of the alkali metal ion with Lewis basic sites on the complex facilitate isolation of the doubly reduced states.

4 The capacity of the BIAN reservoir for electron storage allows for a clean, sequential progression through paramagnetic → diamagnetic → paramagnetic → diamagnetic species (**1** → **2** → **3** → **4**) as judged by EPR and NMR experiments.

5 The 2-electron reduced species exhibits a primarily organic radical that is delocalized into the BIAN glyoxime ligand.

6 CV experiments demonstrate that the DMF solvato species of **1**, namely **1**·$(DMF)_2$, catalyzes the reduction of H^+ to H_2 (confirmed by GC detection in BE). However, the negative potentials associated with this catalytic activity and the associated H^+ reduction activity of the glassy carbon rod WE preclude our ability to discern catalysis by the complex from the electrode in bulk electrolysis measurements.

7 The available resonance forms between the ligand framework and the cobalt metal center prevent proton reduction at potentials that are usually observed for cobaloximes.

8 Overall, the potential utility of the BIAN fragment to serve as an electron reservoir motif for multi-electron catalysis is evident.

4. Experimental

4.1 Reagents and procedures

Cobalt(II) acetate, potassium graphite, sodium metal, mercury, and cobaltocene were purchased from Strem Chemicals. Acenaphthenequinone, hydroxylamine hydrochloride, boron trifluoride etherate, naphthalene, dibenzo-18-crown-6, 18-crown-6 and 12-crown-4 were purchased from Acros Organics and used as received. The ligand $aqdH_2$ was synthesized according to the published procedure of Satake *et al.*[52] All solvents used in the syntheses were purchased from Fisher Scientific, and dry solvents were obtained using a Pure Process Technology solvent purification system. Anhydrous DMF was purchased from Acros Organics and used without further purification for all the electrochemical studies.

4.2 Synthesis of metal complexes

4.2.1 $[Co(aqdBF_2)_2(MeCN)_0]$ (1). Complex **1** was prepared by using a method that is similar to that described by Bakac and Espenson.[38] A 50 mL Schlenk flask was charged with (0.50 g, 2.8 mmol) of acenaphthenequinone dioxime and (0.30 g; 1.2 mmol) of $Co(OAc)_2{\cdot}4H_2O$, and placed under vacuum for 20 min. Dry Et_2O (30 mL) was added, thereby generating a light brown slurry. Next, 1.5 mL of $BF_3{\cdot}Et_2O$ was added *via* syringe. After stirring the reaction mixture for 12 hours, the resulting dark brown precipitate was collected by subsequent filtration. The brown/red powder that had formed was stirred in 20 mL of MeCN for one hour. Subsequent filtration resulted in the isolation of a bright red powder of **1**: 0.249 g; 0.378 mmol; 31.5%. IR (cm^{-1}): 3603 (m), 3530 (m), 1623 (m) 1484 (w) 1416 (w), 1134 (s), 987 (s), 965 (s), 911 (s), 826 (s), 775 (s), 539 (m), 508 (m). UV/Vis in THF, λ_{max} (nm): 505, 340, 280 μ_{eff} = 1.71 μ_B. EPR: g_x = 2.29, g_y = 2.20, g_z = 2.02, 85 K, solid powder (Fig. 6). Elem. Analys. for $C_{28}H_{18}B_2CoF_4N_6O_4$ (%) calcd: C 51.03, H 2.75, N 12.75; found: C 50.98, H 2.63 N 12.37. HR-MS for $[1–2MeCN + Na]^+$: calcd, 600.02130; found, 600.02090.

4.2.2 $[Na(12\text{-crown-}4)_2][Co(aqdBF_2)_2(MeCN)]$ (2). Complex **2** was isolated by dissolving 20.7 mg of the parent compound (0.0314 mmol) in 8 mL of THF. Following this, 1.29 equivalents of $Na[C_{10}H_8]$ was added to the reaction mixture from a standard solution (0.3 mL, 0.135 M $Na[C_{10}H_8]$ in THF). The latter solution was allowed to stir for thirty minutes ultimately generating a purple-blue solution. The solvent was removed under reduced pressure and the resulting powder dissolved in acetonitrile, affording a violet solution with a brown precipitate, which was removed by filtration. Vapor diffusion of Et_2O into the latter solution in the presence of excess (100 mg, 0.568 mmol) 12-crown-4 yielded X-ray quality crystals of compound **2**. Yield: 10.5 mg; 0.011 μmol; 34%. IR (cm^{-1}): 2868 (w), 1609 (w), 1519 (w), 1484 (w) 1443 (w), 1411 (w), 1363 (w), 1304 (w), 1244 (w), 1143 (m), 1093 (s), 983 (s), 912 (s), 849 (m), 827 (m), 789 (m). UV/Vis in THF–MeCN (10 : 1), λ_{max} (nm): 560, 770. This complex was unstable upon re-dissolution in CD_3CN. An alternative salt (below) was prepared to obtain a ^1H NMR spectrum of the singly reduced anion.

4.2.3 $[Co(Cp)_2][Co(aqdBF_2)_2(MeCN)]$ (2′). The parent cobaloxime (23.7 mg, 0.036 mmol) was dispersed in MeCN solution. The subsequent addition of 21.3 mg of cobaltocene (0.126 mol) resulted in the generation of a clear violet solution. The latter solution was allowed to stir for thirty minutes, following which, most of the MeCN solvent was removed under reduced pressure. The solution was then subjected to the addition of Et_2O, generating a purple precipitate of **2′**. The resulting filtrate was dissolved in CD_3CN in order to obtain a satisfactory ^1H NMR spectrum (Fig. 7). Yield: 25 mg; 0.031 mmol; 86%. Crystallization of this compound was effected by vapor diffusion of Et_2O into the above-mentioned solution to afford X-ray quality crystals. ^1H NMR: δ = 8.15 ppm, d; J = 6.8 Hz; δ = 7.92 ppm, d; J = 8.0 Hz, δ = 7.56 ppm, dd; J = 6.8, 8.0 Hz; δ = 5.52 ppm, singlet. Elem. Analys. for $C_{36}H_{25}B_2Co_2F_4N_5O_4$ (%) calcd: C 53.57, H 3.12, N 8.68; found: C 53.69, H 3.08 N 8.62.

4.2.4 $[K(\text{dibenzo-18-crown-6})]_2[Co(aqdBF_2)_2]$ (3). Complex **3** was synthesized by dissolving 22.4 mg of the parent compound (0.034 mmol) in 8 mL of THF. After the addition of 3.2 equivalents of KC_8 (15 mg; 0.111 mmol), the resulting solution was allowed to stir for thirty minutes and filtered to remove any remaining traces of the reductant. To this solution 3.7 equivalents of dibenzo-18-crown-6 (45 mg; 0.125 mmol) were added, resulting in a slight color shift from deep navy blue to a dark blue-green. The solvent was then removed under reduced pressure and the resulting powder was dissolved in acetonitrile, which retained the blue-green hue observed in THF solution. Vapor diffusion of Et_2O into the latter solution afforded a crop of X-ray quality crystals of the desired compound. Crystalline Yield: 21 mg; 0.015 mmol; 45%. IR (cm^{-1}): 2929 (w), 1587 (m), 1504 (s), 1452 (m) 1248 (s), 1213 (s), 1124 (s), 993 (s), 942 (s), 813 (m), 766 (m), 743 (s). UV/Vis in THF, λ_{max} (nm): 605 (broad), 770 (broad). EPR: see text and Fig. 8. This complex proved too unstable for extended times in the solid state to obtain satisfactory elemental analysis.

4.2.5 [K(18-crown-6)]$_2$[Co(aqdBF$_2$)$_2$] (3′). The complex 3′ was synthesized by a similar procedure as for **3**, with 21.6 mg of 1 (0.033 mmol) and 3.1 equivalents of KC_8 (13.7 mg; 0.102 mmol). Following filtration to remove the reducing equivalents, excess 18-crown-6 was added to the solution (34.9 mg; 0.132 mmol). Crystallization of this compound was achieved directly from the above THF solution at reduced temperatures (−20° C) in an argon atmosphere. Crystalline Yield: 16 mg; 0.014 mmol; 41%. IR (cm^{-1}): 2882 (m), 1601 (m), 1520 (m), 1473 (w) 1410 (w), 1352 (m), 1250 (w), 1109 (s), 1060 (m), 1008 (s), 825 (m), 778 (s). This complex proved too unstable for extended times in the solid state to obtain satisfactory elemental analysis.

4.3 Electrochemistry

Cyclic voltammograms and bulk electrolysis experiments were carried out using a Pine Wavenow potentiostat. All CV experiments were performed in a 0.1 M *n*-tetrabutylammonium hexafluorophosphate (NBu_4PF_6)–*N*,*N*-dimethylformamide electrolyte solution equipped with a glassy carbon button working electrode, a platinum wire counter-electrode, and a silver wire quasi-reference electrode. The resulting potentials are reported with respect to the ferrocene/ferrocenium redox couple (these values can be calculated with respect to SCE by the addition of 0.5 V). The bulk electrolysis measurements were carried out in a custom H-cell with two frits separating the working and counter electrode compartments ($V \approx 50$ mL). Each cell was equipped with a glassy carbon rod (Tokai Carbon) as the working electrode and counter electrode. The silver wire reference electrode was connected to the potentiostat by means of a copper wire. In the H-cell experiments, a pre-charge period of approximately three hours was employed by holding the potentiostat to a potential just cathodic of the second redox peak, thus generating an intense blue solution of the pre-catalyst.

4.4 X-ray crystallography

Structures were solved, refined, and analyzed using standard procedures[53–57] Definitions used for calculating $R(F)$, w$R(F^2)$ and the goodness of fit, S, are given below.[58] All figures were generated using Mercury.[59] Details regarding the data collection and solution parameters for aqdH$_2$ and the cobalt complexes are summarized in Table 1.

4.4.1 [aqdH$_2$]. Crystals were grown by slow evaporation of a solution of aqdH$_2$ in Et$_2$O–hexanes. A single, light yellow crystal was used for data collection, with approximate dimensions 0.114 × 0.106 × 0.094 mm. The data were collected at 25 °C on a Rigaku SCX-Mini diffractometer using a graphite monochromator with MoKα radiation (λ = 0.71073 Å). A total of 920 frames of data were collected using ω and ϕ-scans with a scan range of 1.0° and a counting time of 60.0 seconds per frame. Data reduction was performed using Rigaku Americas Corporations Crystal Clear version 1.40.[60] Details of crystal data, data collection and structure refinement are listed in Table 1. The oxime bound protons were observed in the electron difference map and modeled by a freely rotating riding

Table 1 Crystal data and refinement parameters for the ligand (aqdH$_2$), the parent cobaloxime (**1**), and the reduced complexes (**2**–**3**)

	aqdH$_2$	**1** [Co(aqdBF$_2$)$_2$(MeCN)$_2$]·MeCN	**2** [Na(12-crown-4)$_2$]-[Co(aqdBF$_2$)$_2$(MeCN)]·2(MeCN)	**3** [K(dibenzo(18-crown-6)]$_2$ [Co(aqdBF$_2$)$_2$]·2MeCN·Et$_2$O	**4** [K(18-crown-6)]-2[Co(aqdBF$_2$)$_2$]·2THF
Formula	$C_12H_8N_2O_2$	$C_32H_24B_2CoF_4N_8O_4$	$C_46H_53B_2CoF_4N_7NaO_12$	$C_72H_76B_2CoF_4K_2N_6O_17$	$C_64H_92B_2CoF_4K_2N_4O_20$
FW	212.20	741.14	1075.49	1532.13	1472.16
Color	Yellow	Red	Violet	Deep blue	Deep blue
Habit	Block	Parallelpiped	Shard	Shard	Block
Size (mm)	0.182 × 0.114 × 0.094	0.412 × 0.159 × 0.116	0.371 × 0.224 × 0.170	0.435 × 0.374 × 0.275	0.383 × 0.263 × 0.191
T (K)	298(2)	173(2)	150(2)	150(2)	150(2)
λ (Å)	0.71073 (MoK$_\alpha$)	0.71073 (MoK$_\alpha$)	1.54184 (CuK$_\alpha$)	1.54184 (CuK$_\alpha$)	1.54184 (CuK$_\alpha$)
Lattice	Monoclinic	Monoclinic	Monoclinic	Monoclinic	Monoclinic
space group	P_{21}/c	C_2/m	P_{21}/c	P_{21}/n	P_{21}/c
a (Å)	7.844(3)	8.9648(3)	12.22900(10)	15.568(6)	12.9854(6)
b (Å)	7.8009(29)	18.8380(6)	15.5856(2)	20.730(8)	19.0412(9)
c (Å)	15.3089(59)	9.4411(3)	13.20690(10)	22.817(9)	14.1063(8)
α (Å)	90	90	90	90	90
β (Å)	92.7816(102)	99.3490(10)	98.8380(10)	95.249(7)	93.331(5)
γ (Å)	90	90	90	90	90
V (Å^3)	935.68(62)	1573.22(9)	2487.30(4)	7333(5)	3482.0(3)
Z	2	3	4	5	6
d_{calc} (g cm^{-3})	1.506	1.565	1.436	1.388	1.404
μ (mm^{-1})	0.106	0.623	3.509	3.546	3.725
GOF on F^2	1.105	1.202	0.933	1.045	1.042
R Indices	R_1 = 0.0415	R_1 = 0.0274	R_1 = 0.0447	R_1 = 0.0533	R_1 = 0.0547
[$I > 2\sigma(I)$]	wR_2 = 0.0905	wR_2 = 0.0814	wR_2 = 0.1223	wR_2 = 0.1422	wR_2 = 0.1493
R Indices all data	R_1 = 0.0510	R_1 = 0.0338	R_1 = 0.0480	R_1 = 0.0650	R_1 = 0.0696
	wR_2 = 0.0956	wR_2 = 0.0961	wR_2 = 0.1263	wR_2 = 0.1519	wR_2 = 0.1637

model on the oxime oxygens. They were refined isotropically without restraints.

4.4.2 $[Co(aqdBF_2)_2(MeCN)_2]MeCN$ (1). Crystals were grown by layering acetonitrile over a saturated solution of **1** in THF. A whole parallel piped crystal was used for data collection, with approximate dimensions 0.401 × 0.164 × 0.126 mm. The data were collected at −120 °C on a Nonius Kappa CCD diffractometer using a Bruker AXS Apex II detector and a graphite monochromator with MoKα radiation (λ = 0.71073 Å). Reduced temperatures were maintained by use of an Oxford Cryosystems 600 low-temperature device. A total of 1048 frames of data were collected using ω and ϕ-scans with a scan range of 0.8° and a counting time of 46.24 seconds per frame. Data reduction was performed using SAINT V8.27B.[61] Details of crystal data, data collection and structure refinement are listed in Table 1. The hydrogen atoms on C8 were observed in a ΔF map and refined with isotropic displacement parameters, with the hydrogen sitting on the mirror plane assigned a site occupancy factor of 0.5. All other hydrogen atoms were affixed to the carbons with an appropriate riding model.

4.4.3 $[Na(12\text{-crown-}4)_2][Co(aqdBF_2)_2(MeCN)]$ (2). Crystals of **2** were grown by vapor diffusion of Et_2O into a saturated solution of the above complex in MeCN. A dark purple fragment was broken away from a large crystal and used for data collection, with approximate dimensions 0.371 × 0.224 × 0.170 mm. The data were collected at −123 °C on a Agilent Technologies SuperNova diffractometer using an Atlas S2 Detector and CuKα radiation (λ = 1.54184 Å). Reduced temperatures were maintained by use of an Oxford Cryosystems 700 low-temperature device. A total of 1053 frames of data were collected using ω-scans with a scan range of 1.0° and a counting time of 1.0–4.5 seconds per frame. Data reduction was performed using CrysAlisPro.[62] Details of crystal data collection and structure refinement are listed in Table 1. One of the crown-ether molecules was refined without bonds to symmetry generated atoms *via* a PART-1 instruction card. The alternate crown was modelled with positional disorder in the ethylene bridging units. All non-hydrogen atoms were refined anisotropically, solvent molecules and disordered crown ether atoms were refined with UDP, but not positional restraint.

4.4.4 $[K(dibenzo\text{-}18\text{-crown-}6)]_2[Co(aqdBF_2)_2]$ (3). Crystals of **3** were grown by vapor diffusion of Et_2O into a saturated solution of the above complex in MeCN. A dark blue shard was used for data collection, with approximate dimensions 0.435 × 0.374 × 0.275 mm. The data were collected at −123 °C on a Agilent Technologies SuperNova diffractometer using an Atlas S2 Detector and CuKα radiation (λ = 1.54184 Å). Reduced temperatures were maintained by use of an Oxford Cryosystems 700 low-temperature device. A total of 1031 frames of data were collected using ω-scans with a scan range of 1.0° and a counting time of 1.0–20 seconds per frame. Data reduction was performed using CrysAlisPro.[62] Details of crystal data, data collection and structure refinement are listed in Table 1. All non-hydrogen atoms were refined anisotropically and without restraint with the exception of a rigid bond (RIGU) restraint on the solvent ether molecule.

4.4.5 $[K(18\text{-crown-}6)]_2[Co(aqdBF_2)_2]$ (3′). Crystals of **3′** were grown at reduced temperature (−20 °C) from a saturated THF solution. A blue shard was used for data collection, with approximate dimensions 0.383 × 0.263 × 0.191 mm. The data were collected at 133 K on a Agilent Technologies SuperNova diffractometer using an Atlas S2 Detector and CuKα radiation (λ = 1.54184 Å). Reduced temperatures were maintained by use of an Oxford Cryosystems 700 low-temperature device. A total of 682 frames of data were collected using ω-scans with a scan range of 1.0° and a counting time of 1.0–15 seconds per frame. Data reduction was performed using CrysAlisPro.[62] Details of crystal data, data collection and structure refinement are listed in Table 1. All non-hydrogen atoms were refined anisotropically and without restraint.

4.5 Physical measurements

EPR spectra were obtained on a Bruker Biospin EMXplus 114 X-band spectrometer with a liquid nitrogen variable temperature cryostat. Infrared spectra were recorded using a Bruker Alpha spectrometer equipped with a diamond ATR crystal. ^1H NMR spectra were collected on a Varian DirecDrive 400 MHz spectrometer. UV/vis absorption spectra were obtained at 298 K using an Ocean Optics fiber optic system equipped with a low intensity PX-2 pulsed xenon lamp and a USB2000-XR1-ES detector; samples were prepared as 0.1 mM solutions of the complexes in THF in 1 cm quartz cuvettes. Solid state magnetic susceptibilities were measured at 298 K with a Johnson Matthey Mark I instrument.

4.6 Gas chromatography product analysis

Gas samples (5 mL) were drawn from the bulk electrolysis cell by means of a Vici gas tight syringe (Cat # 050055). The samples were injected into a Shimadzu GC-2014 Fuel Cell Analyzer gas chromatograph, with an argon gas mobile phase. The products were analyzed on a dual sensor system equipped with a thermal conductivity detector and a flame ionization detector.

4.7 DFT calculations

Geometry optimizations were performed on **1**, **2**, and **3** using the coordinates obtained from the crystal structure as starting point. A Hessian calculation that was performed on the optimized structures showed no imaginary frequencies. The Firefly software package[63] was utilized in conjunction with the B3P86 functional and the 6-31G(d,p) basis set with diffuse functions on heteroatoms and the cobalt center. A larger basis set was used to perform energy calculations, consisting of the Wachters basis set for the cobalt center and the TZVP basis set of Barbieri *et al.* for the remaining atoms.[64,65] Orbitals and spin density plots were visualized and rendered using Chemcraft.[66] Initially, spin density calculations on the doubly reduced species **3** were performed with no restrictions, however, this lead to spin contamination (S^2 = 1.038). Thus, the results displayed are those of a restricted open shell calculation.

Acknowledgements

The authors thank the Robert A. Welch Foundation (F-0003, AHC; F-1822, MJR), ACS Petroleum Research Fund (PRF 53542-DN13), UT Austin College of Natural Sciences, and the Office of Naval Research (N00014-13-10530) for financial support. We also thank Dr Vincent Lynch for assistance with crystallography, and Mr Mike Ronalter and Mr Adam Kennedy for expertise in custom glassware fabrication.

Notes and references

1 E. E. Benson, C. P. Kubiak, A. J. Sathrum and J. M. Smieja, *Chem. Soc. Rev.*, 2008, **38**, 89–99.
2 A. J. Morris, G. J. Meyer and E. Fujita, *Acc. Chem. Res.*, 2009, **42**, 1983–1994.
3 M. Rakowski Dubois and D. L. Dubois, *Acc. Chem. Res.*, 2009, **42**, 1974–1982.
4 H. Dau, C. Limberg, T. Reier, M. Risch, S. Roggan and P. Strasser, *ChemCatChem*, 2010, **2**, 724–761.
5 P. Du and R. Eisenberg, *Energy Environ. Sci.*, 2012, **5**, 6012–6021.
6 V. S. Thoi, Y. Sun, J. R. Long and C. J. Chang, *Chem. Soc. Rev.*, 2013, **42**, 2388–2400.
7 J. L. Dempsey, B. S. Brunschwig, J. R. Winkler and H. B. Gray, *Acc. Chem. Res.*, 2009, **42**, 1995–2004.
8 V. Artero, M. Chavarot-Kerlidou and M. Fontecave, *Angew. Chem., Int. Ed.*, 2011, **50**, 7238–7266.
9 R. Dreos, S. Geremia, G. Nardin, L. Randaccio, G. Tauzher and S. Vuano, *Inorg. Chim. Acta*, 1998, **272**, 74–79.
10 X. Hu, B. M. Cossairt, B. S. Brunschwig, N. S. Lewis and J. C. Peters, *Chem. Commun.*, 2005, 4723–4725.
11 M. Razavet, V. Artero and M. Fontecave, *Inorg. Chem.*, 2005, **44**, 4786–4795.
12 X. Hu, B. S. Brunschwig and J. C. Peters, *J. Am. Chem. Soc.*, 2007, **129**, 8988–8998.
13 C. Baffert, V. Artero and M. Fontecave, *Inorg. Chem.*, 2007, **46**, 1817–1824.
14 B. H. Solis and S. Hammes-Schiffer, *Inorg. Chem.*, 2011, **50**, 11252–11262.
15 B. H. Solis, Y. Yu and S. Hammes-Schiffer, *Inorg. Chem.*, 2013, **52**, 6994–6999.
16 A. Bhattacharjee, M. Chavarot-Kerlidou, J. L. Dempsey, H. B. Gray, E. Fujita, J. T. Muckerman, M. Fontecave, V. Artero, G. M. Arantes and M. J. Field, *ChemPhysChem*, 2014, **15**, 2951–2958.
17 J. Niklas, K. L. Mardis, R. R. Rakhimov, K. L. Mulfort, D. M. Tiede and O. G. Poluektov, *J. Phys. Chem. B*, 2012, **116**, 2943–2957.
18 J. L. Dempsey, J. R. Winkler and H. B. Gray, *J. Am. Chem. Soc.*, 2010, **132**, 1060–1065.
19 J. L. Dempsey, J. R. Winkler and H. B. Gray, *J. Am. Chem. Soc.*, 2010, **132**, 16774–16776.
20 L. A. Berben and J. C. Peters, *Chem. Commun.*, 2010, **46**, 398–400.
21 Z. Ji, M. He, Z. Huang, U. Ozkan and Y. Wu, *J. Am. Chem. Soc.*, 2013, **135**, 11696–11699.
22 E. S. Andreiadis, P.-A. Jacques, P. D. Tran, A. Leyris, M. Chavarot-Kerlidou, B. Jousselme, M. Matheron, J. Pcaut, S. Palacin, M. Fontecave and V. Artero, *Nat. Chem.*, 2013, **5**, 48–53.
23 A. Krawicz, J. Yang, E. Anzenberg, J. Yano, I. D. Sharp and G. F. Moore, *J. Am. Chem. Soc.*, 2013, **135**, 11861–11868.
24 A. Krawicz, D. Cedeno and G. F. Moore, *Phys. Chem. Chem. Phys.*, 2014, **16**, 15818–15824.
25 A. Fihri, V. Artero, A. Pereira and M. Fontecave, *Dalton Trans.*, 2008, 5567–5569.
26 P. Zhang, M. Wang, C. Li, X. Li, J. Dong and L. Sun, *Chem. Commun.*, 2009, 8806–8808.
27 T. M. McCormick, B. D. Calitree, A. Orchard, N. D. Kraut, F. V. Bright, M. R. Detty and R. Eisenberg, *J. Am. Chem. Soc.*, 2010, **132**, 15480–15483.
28 G.-G. Luo, K. Fang, J.-H. Wu, J.-C. Dai and Q.-H. Zhao, *Phys. Chem. Chem. Phys.*, 2014, **16**, 23884–23894.
29 B. D. Stubbert, J. C. Peters and H. B. Gray, *J. Am. Chem. Soc.*, 2011, **133**, 18070–18073.
30 C. C. L. McCrory, C. Uyeda and J. C. Peters, *J. Am. Chem. Soc.*, 2012, **134**, 3164–3170.
31 X. Yin, C. Liu, S. Zhuo, Y. Xu and B. Zhang, *Dalton Trans.*, 2014, **44**, 1526–1529.
32 S. Troppmann and B. Knig, *Chem. – Eur. J.*, 2014, **20**, 14570–14574.
33 M. Bacchi, G. Berggren, J. Niklas, E. Veinberg, M. W. Mara, M. L. Shelby, O. G. Poluektov, L. X. Chen, D. M. Tiede, C. Cavazza, M. J. Field, M. Fontecave and V. Artero, *Inorg. Chem.*, 2014, **53**, 8071–8082.
34 C. N. Valdez, J. L. Dempsey, B. S. Brunschwig, J. R. Winkler and H. B. Gray, *Proc. Natl. Acad. Sci. U. S. A.*, 2012, **109**, 15589–15593.
35 P. Kelley, M. W. Day and T. Agapie, *Eur. J. Inorg. Chem.*, 2013, **2013**, 3840–3845.
36 S. M. Laga, J. D. Blakemore, L. M. Henling, B. S. Brunschwig and H. B. Gray, *Inorg. Chem.*, 2014, **53**, 12668–12670.
37 G. N. Schrauzer and R. J. Windgassen, *Chem. Ber.*, 1966, **99**, 602–610.
38 A. Bakac and J. H. Espenson, *J. Am. Chem. Soc.*, 1984, **106**, 5197–5202.
39 M. J. Rose, H. B. Gray and J. R. Winkler, *J. Am. Chem. Soc.*, 2012, **134**, 8310–8313.
40 R. van Asselt and C. J. Elsevier, *Tetrahedron*, 1994, **50**, 323–334.
41 I. L. Fedushkin, A. A. Skatova, V. A. Chudakova and G. K. Fukin, *Angew. Chem., Int. Ed.*, 2003, **42**, 3294–3298.
42 K. Vasudevan and A. H. Cowley, *Chem. Commun.*, 2007, 3464–3466.
43 K. V. Vasudevan, M. Findlater, I. Vargas-Baca and A. H. Cowley, *J. Am. Chem. Soc.*, 2012, **134**, 176–178.
44 I. L. Fedushkin, O. V. Maslova, A. G. Morozov, S. Dechert, S. Demeshko and F. Meyer, *Angew. Chem., Int. Ed.*, 2012, **51**, 10584–10587.

45 P. Mondal, H. Agarwala, R. D. Jana, S. Plebst, A. Grupp, F. Ehret, S. M. Mobin, W. Kaim and G. K. Lahiri, *Inorg. Chem.*, 2014, **53**, 7389–7403.
46 N. J. Hill, I. Vargas-Baca and A. H. Cowley, *Dalton Trans.*, 2008, 240–253.
47 N. G. Connelly and W. E. Geiger, *Chem. Rev.*, 1996, **96**, 877–910.
48 V. Fourmond, P.-A. Jacques, M. Fontecave and V. Artero, *Inorg. Chem.*, 2010, **49**, 10338–10347.
49 B. D. McCarthy, D. J. Martin, E. S. Rountree, A. C. Ullman and J. L. Dempsey, *Inorg. Chem.*, 2014, **53**, 8350–8361.
50 E. Anxolabhre-Mallart, C. Costentin, M. Fournier, S. Nowak, M. Robert and J.-M. Savant, *J. Am. Chem. Soc.*, 2012, **134**, 6104–6107.
51 E. Anxolabre-Mallart, C. Costentin, M. Fournier and M. Robert, *J. Phys. Chem. C*, 2014, **118**, 13377–13381.
52 M. Satake, J. Miura, S. Usami and B. K. Puri, *Analyst*, 1989, **114**, 813–818.
53 M. C. Burla, R. Caliandro, M. Camalli, B. Carrozzini, G. L. Cascarano, L. De Caro, C. Giacovazzo, G. Polidori and R. Spagna, *J. Appl. Crystallogr.*, 2005, **38**, 381–388.
54 G. M. Sheldrick, *Acta Crystallogr., Sect. A: Fundam. Crystallogr.*, 2008, **64**, 112–122.
55 A. L. Spek, *Acta Crystallogr., Sect. D: Biol. Crystallogr.*, 2009, **65**, 148–155.
56 L. J. Farrugia, *J. Appl. Crystallogr.*, 2012, **45**, 849–854.
57 A. J. C. Wilson, *International Tables for X-ray Crystallography*, Kluwer Academic Press, Boston, 1992, vol. C.
58 $R_w(F^2) = \sqrt{\frac{\Sigma w(|F_o|^2 - |F_c|^2)^2}{\Sigma w(|F_o|)^4}}$, where w is the weight given each reflection. $R(F) = \frac{\Sigma(|F_o| - |F_c|)}{\Sigma|F_o|}$ for reflections with $F_o > 4(\sigma(F_o))$. GOF, $S = \sqrt{\frac{\Sigma w(|F_o|^2 - |F_c|^2)^2}{(n-p)}}$, where n is the number of reflections and p is the number of refined parameters.
59 C. F. Macrae, I. J. Bruno, J. A. Chisholm, P. R. Edgington, P. McCabe, E. Pidcock, L. Rodriguez-Monge, R. Taylor, J. van de Streek and P. A. Wood, *J. Appl. Crystallogr.*, 2008, **41**, 466–470.
60 *CrystalClear-SM v. 1.4.0 SP1*, Rigaku Americas Corporation, 1998–2008.
61 *SAINT v. 8.27B*, Bruker AXS Inc, Madison, WI, 2012.
62 *CrysAlisPro. Agilent Technologies*, Agilent Technologies UK Ltd., Oxford, UK, 2013, SuperNova CCD System, CrysAlisPro Software System, 1.171.37.31.
63 A. Granovsky, Firefly v. 8.0.0, http://classic.chem.msu.su.
64 A. J. H. Wachters, *J. Chem. Phys.*, 1970, **52**, 1033–1036.
65 P. L. Barbieri, P. A. Fantin and F. E. Jorge, *Mol. Phys.*, 2006, **104**, 2945–2954.
66 G. Andrienko, Chemcraft v. 1.8, http://www.chemcraftprog.com.